Magnetism and Faraday Rotation in Oxygen-Deficient Polycrystalline and Single-Crystal Iron-Substituted Strontium Titanate

Taichi Goto,[1,*] Dong Hun Kim,[2] Xueyin Sun,[3] Mehmet C. Onbasli,[4] Juan M. Florez,[5] Shyue Ping Ong,[6] Patricio Vargas,[5] Karl Ackland,[7] Plamen Stamenov,[7] Nicolas M. Aimon,[4] Mitsuteru Inoue,[1] Harry L. Tuller,[4] Gerald F. Dionne,[4] J. Michael D. Coey,[7] and Caroline A. Ross[4,†]

[1]*Department of Electrical and Electronic Information Engineering, Toyohashi University of Technology, 1-1 Hibari-Ga-Oka, Tempaku, Toyohashi 441-8580, Japan*
[2]*Department of Materials Science and Engineering, Myongji University, 116 Myongji-ro, Cheoin-gu, Yongin, Kyeonggi-do 449-728, Korea*
[3]*School of Materials Science and Engineering, Harbin Institute of Technology, 92 West Dazhi Street, Nan Gang District, Harbin 150001, China*
[4]*Department of Materials Science and Engineering, Massachusetts Institute of Technology, 77 Massachusetts Avenue, Cambridge, Massachusetts 02139, USA*
[5]*Departamento de Física, Universidad Técnica Federico Santa María, España 1680, Valparaíso, P.O. Box 110-V, Chile*
[6]*Department of NanoEngineering, University of California, San Diego, 9500 Gilman Drive, La Jolla, California 92093, USA*
[7]*School of Physics, Trinity College Dublin, College Green, Dublin 2, Ireland*

(Received 18 May 2016; revised manuscript received 31 October 2016; published 8 February 2017)

Both polycrystalline and single-crystal films of iron-substituted strontium titanate, $Sr(Ti_{0.65}Fe_{0.35})O_{3-\delta}$, prepared by pulsed laser deposition, show room-temperature magnetism and Faraday rotation, with the polycrystalline films exhibiting higher saturation magnetization and Faraday rotation. The magnetic properties vary with the oxygen pressure at which the films are grown, showing a maximum at pressures of approximately 4 μ Torr at which the unit-cell volume is largest. The results are discussed in terms of the oxygen stoichiometry and corresponding Fe valence states, the structure and strain state, and the presence of small-volume fractions of metallic Fe in single-crystal films grown at the optimum deposition pressure. Integration of magneto-optical polycrystalline films on an optical-waveguide device demonstrates a nonreciprocal phase shift.

DOI: 10.1103/PhysRevApplied.7.024006

I. INTRODUCTION

Complex oxides exhibit a wide range of useful properties such as high-temperature superconductivity, ferroelectricity, colossal magnetoresistance, magnetism, magnetoelectricity, magneto-optical activity, and multiferroicity that have inspired spintronic, magnetoelectronic, and optical applications [1–6]. Transition-metal-substituted perovskites or perovskite-derived structures are particularly interesting because their properties can be tuned by cation substitution over extensive composition ranges, and because they can be epitaxially grown on a buffered Si substrate [7–10]. Beyond cation composition, the properties are also very sensitive to the growth conditions and substrate used, which affect the microstructure, film strain [7], oxygen deficiency, the cation valence states, and the ordering of cations within the A and B sites.

Iron-substituted strontium titanate or $SrTi_{1-x}Fe_xO_{3-\delta}$ (STF) (here δ represents the oxygen deficiency with respect to a stoichiometric perovskite $SrTi_{1-x}Fe_xO_3$, i.e., one in which the Fe is present as Fe^{4+}) has been extensively characterized as a mixed electronic-ionic conductor [11–15] and for its magnetic, magneto-optical, ferroelectric, and catalytic properties [16–19]. Characterization of STF has included determining its oxygen content via thermogravimetric analysis and coulometric titration [20,21], and measurements of ionic and electronic conductivity and impedance [12,13,15,22–24]. The magnetic properties are believed to be related to oxygen vacancies [16,20,25], although the origin of the magnetism is not fully understood. We have previously found that epitaxial STF and $Sr(Ti_{1-x}Co_x)O_{3-\delta}$ (STCo) films on $SrTiO_3$ (STO), $LaAlO_3$, and CeO_2/yttria-stabilized-zirconia-(YSZ) buffered (001) Si substrates grown in vacuum with $x = 0.1$ to 0.5, i.e., nondilute systems, exhibited room-temperature magnetism and anisotropy with an out-of-plane magnetic easy axis that was attributed to magnetoelastic effects [16,17,26–28]. However, films deposited in oxygen had no significant room-temperature magnetism. The magnetic moment of vacuum-deposited epitaxial STF films persisted to a temperature of >1000 °C

*goto@ee.tut.ac.jp
†caross@mit.edu

and the magnetization decreased slowly as a function of temperature [16,29,30]. Depending on the thickness and deposition conditions, STF could be grown as a single-crystal film on STO, or as a double-epitaxial film consisting of an (001)-oriented STF film with (011)-oriented crystals growing within it, both orientations being epitaxial with the substrate [31]. The single-crystal and double-epitaxial microstructures differed in their strain state, uniformity of the Fe distribution, and magnetic properties [19,31].

These experimental results led to the conclusion that strain and oxygen stoichiometry were key factors in determining the magnetic properties of the STF and STCo films (factors that are also important in many other oxide systems [29,32]), but there are few reports on the effect of oxygen pressure during growth [33,34], and polycrystalline films have not been investigated. We report on the correlations among the microstructure, valence, and distribution of the Fe ions as well as the room-temperature magnetic properties of STF films as a function of base pressure P, characterized by high-resolution x-ray diffraction (XRD), transmission electron microscopy (TEM), Faraday rotation (FR), magnetometry, and Mössbauer spectroscopy. The STF films on Si were polycrystalline but exhibited a magnetic moment and FR up to 65% higher than the single-crystal film deposited on an STO substrate. From the viewpoint of applications, the formation of polycrystalline magnetic perovskite films on silica or other nonepitaxial substrates allows the useful properties of STF to be easily introduced into complementary metal-oxide semiconductor devices and into optical devices such as isolators and magnetophotonic crystals [4,35–39], spatial light modulators [40–42], or magneto-optical holographic memories [43–46]. First-principles calculations demonstrate the importance of oxygen defects and exchange interactions in determining the magnetic properties.

II. FILM GROWTH AND CHARACTERIZATION

A. Film preparation

In this work, STF films are fabricated on silicon covered by a native oxide and on STO substrates under various P using pulsed laser deposition (PLD). The $SrTi_{0.62}Fe_{0.38}O_{3-\delta}$ target is prepared using a conventional mixed oxide sintering method [47]. During film deposition, the KrF excimer laser (wavelength $\lambda = 248$ nm) is pulsed at a frequency of 10 Hz with a pulse duration of 25 ns. The spot size on the target is 0.5 mm × 2.0 mm, and the energy density at the target surface is approximately 1.3 $J\,cm^{-2}$ during the pulse. The deposition rate is 1.8–2.7 $nm\,min^{-1}$. STF films of thickness 70 ± 10 nm are deposited by PLD onto 0.38-mm-thick double-side-polished (001) Si substrates and onto 0.5-mm-thick double-side-polished (001) STO substrates. Films are grown simultaneously on both substrate types in each deposition run. The substrates are placed 80 mm from the target, and the substrate holder is heated to 650 °C and is rotated for uniform growth. This temperature is chosen to minimize the formation of secondary phases such as iron oxides. Samples are prepared at a range of base pressures below 10 μTorr by pumping the chamber until a specific base pressure P is reached. The substrate is then heated, which raises the total pressure of the chamber to about 30 μTorr due to chamber outgassing. The chamber pressure is then pumped back down to P before deposition starts. Therefore, the pressure P during deposition consists of residual gas which includes oxygen and water vapor. Predeposition (5×10^3 laser pulses) is started with the shutter placed between the PLD target and the substrate, leading to an increase in the total chamber pressure by approximately 2 μTorr. After opening the shutter for film deposition (2×10^4 pulses), the chamber pressure gradually decreases and returns to near P at the end of the deposition. The substrate is cooled to room temperature at a rate of $-5\,°C\,min^{-1}$ while pumping the chamber.

B. X-ray characterization

In-plane and out-of-plane lattice constants of single-crystal films on STO and polycrystalline films on Si are characterized by XRD (PANalytical, X'Pert) and two high-resolution XRD systems (HRXRD, Bruker-AXS D8 DISCOVER, and Rigaku Smartlab). XRD patterns are shown in Figs. 1(a) and 1(b) for STF/STO and STF/Si, taken using a Cu-Kα radiation source at a wavelength of 0.154 18 nm. Figure 1(a) is measured by XRD (PANalytical, X'Pert), in which Kβ_1 peaks from the Cu source are observed. Figure 1(b) is measured by HRXRD (Rigaku Smartlab). The STF/Si samples are tilted by 1° to eliminate the strong substrate peak. The out-of-plane lattice parameters of STF on STO and on Si, $c_{STF/STO}$ and $c_{STF/Si}$, vary with the deposition pressure, and exhibit a maximum at $P = 3$–4 μTorr, with the variation stronger for the STF/STO. This behavior is also confirmed with the (002) peak obtained from XRD (PANalytical X'Pert). The TiO_2 (202) peak in Fig. 1(a) originates from the substrate.

Reciprocal space mapping (RSM) is used to measure the in-plane lattice parameter $a_{STF/STO}$ for the STF/STO. Grazing-incidence diffraction was used to measure $a_{STF/Si}$ for the STF/Si samples grown at $P = 1$, 4, and 10 μTorr with the incident angle of the x rays ω fixed at 0.4°. Figure 1(c) shows the RSM data for the STF/STO samples for the asymmetric (310) peak. The intense upper peak arises from diffraction from the STO substrate, and the bottom peak corresponds to the STF films. Multiple peaks are attributed to twinning of the substrates. The film and substrate peaks align in q_x indicating coherent cube-on-cube epitaxial growth of the STF films on the STO substrate, i.e., $a_{STF/STO} = a_{STO}$, whereas q_z gives the out-of-plane lattice parameter c, which differs for the film and substrate. The RSM data gave a standard deviation of

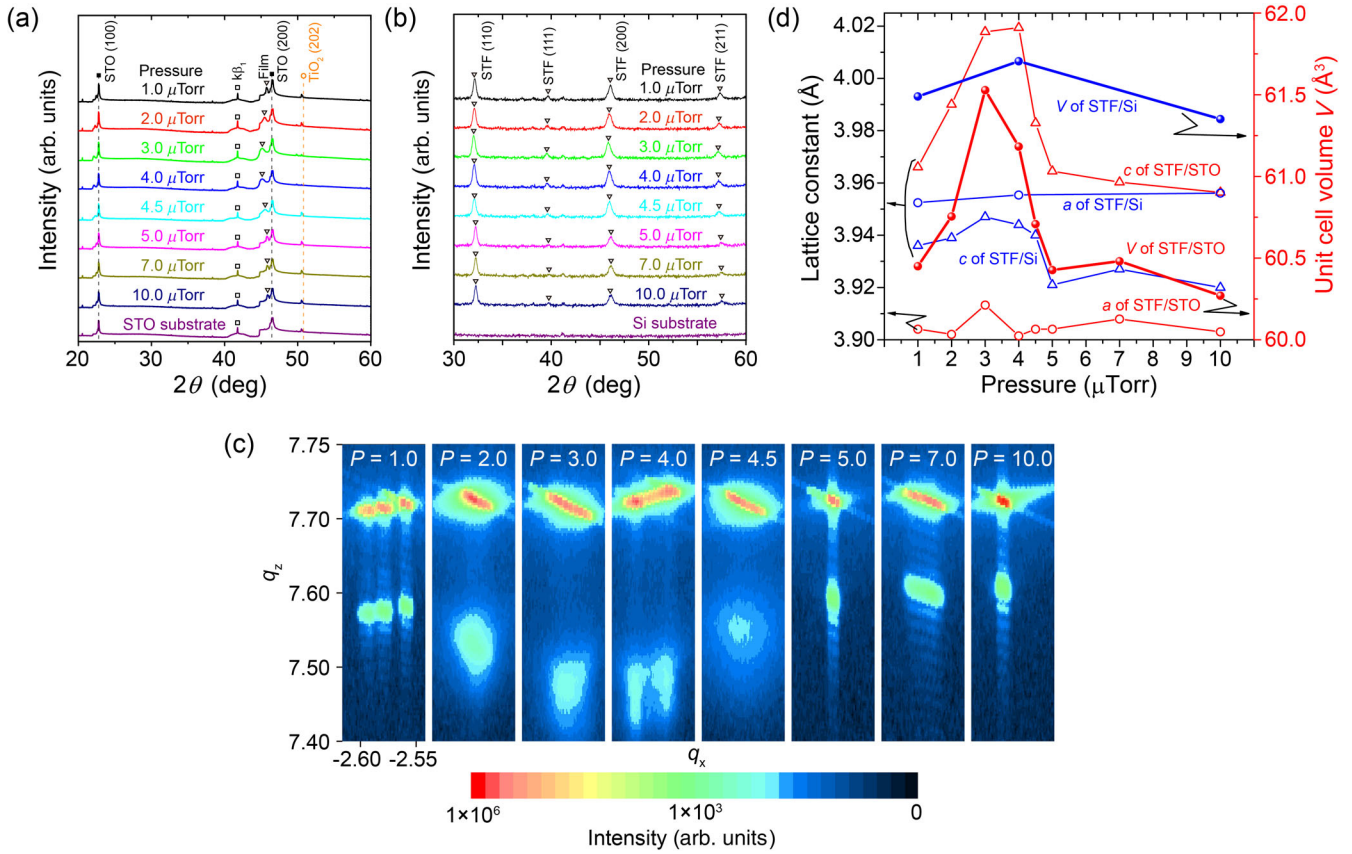

FIG. 1. Structural analysis of the STF films with XRD. (a) XRD patterns of STF/STO. The triangles show the film peaks. Black squares are peaks from bulk STO. A circle shows a TiO_2 peak present in the substrate scan. (b) XRD patterns of STF/Si. Positions of STF peaks are shown with triangles. There are no Si peaks in this angular range. (c) Reciprocal space mapping of single-crystal STF on STO substrate, plotted in $q_z - q_x$ for the asymmetric (310) peak. (d) Lattice constants and unit-cell volumes of STF films versus deposition pressure for both STF/STO and STF/Si.

$<10^{-3}$ Å for $a_{\mathrm{STF/STO}}$. The difference in values for c from different diffractometers, given by (HRXRD value–XRD value)/HRXRD value, is less than 0.1%, and the value of $c_{\mathrm{STF/STO}}$ from RSM matches that measured by XRD. All the STF films on STO had out-of-plane lattice parameters greater than that of STO ($a_{\mathrm{STO}} = 3.905$ Å) and are tetragonally distorted, with $(c/a)_{\mathrm{STF/STO}} = 1.013$ to 1.030 indicating an in-plane compressive strain in the STF, similar to that found in prior work [16]. Figure 1(d) shows the variation of $a_{\mathrm{STF/STO}}$, $c_{\mathrm{STF/STO}}$, and unit-cell volume $V_{\mathrm{STF/STO}}$ with base pressure P.

For the samples of STF/Si, the in-plane and out-of-plane lattice parameters, $a_{\mathrm{STF/Si}}$ and $c_{\mathrm{STF/Si}}$, and the unit-cell volume $V_{\mathrm{STF/Si}}$ are shown in Fig. 1(d). The data gave a standard deviation of approximately 6×10^{-4} Å for a, and 2×10^{-3} Å for c. The value of $a_{\mathrm{STF/Si}}$ is 3.955 ± 0.003 Å and shows little variation with P. Of the three STF/Si samples whose unit-cell volume is measured, the one grown at $P = 4.0$ μTorr shows the largest unit-cell volume, the same trend as for films on the STO substrate. The value of $c_{\mathrm{STF/Si}}$ is similar to or slightly smaller than $a_{\mathrm{STF/Si}}$, i.e., $(c/a)_{\mathrm{STF/Si}} = 0.990$ to 0.998, depending on P. Thermal mismatch on cooling would lead to a tensile strain in the STF/Si film ($c/a < 1$), since Si has a lower thermal expansion coefficient than STF. This differs from the films on STO where lattice mismatch governs the strain state and produces an in-plane compressive strain in the STF, with $c/a > 1$.

The larger unit-cell volume of the films compared to that estimated for bulk STF without oxygen vacancies [$SrTi_{0.65}Fe_{0.35}O_3$, $V = \sim 60.13$ Å^3 interpolated linearly from the unit-cell volumes of STO ($a = 3.9051$ Å, $V = \sim 59.55$ Å^3) [48] and $SrFeO_3$ ($a = 3.9410$ Å, $V = \sim 61.21$ Å^3) [49]] is a result of the greater oxygen vacancy content in the films compared to the bulk, which drives the Fe to lower valence states, expanding the lattice because of the larger ionic radii of the Fe. Other work on STO films [50] has shown changes in cation stoichiometry and hence lattice parameter at different laser focus conditions, but here we keep the deposition conditions nominally the same except for the base pressure, so we attribute changes in lattice volume to the oxygen vacancies and corresponding changes in Fe ionic radius. MacChesney

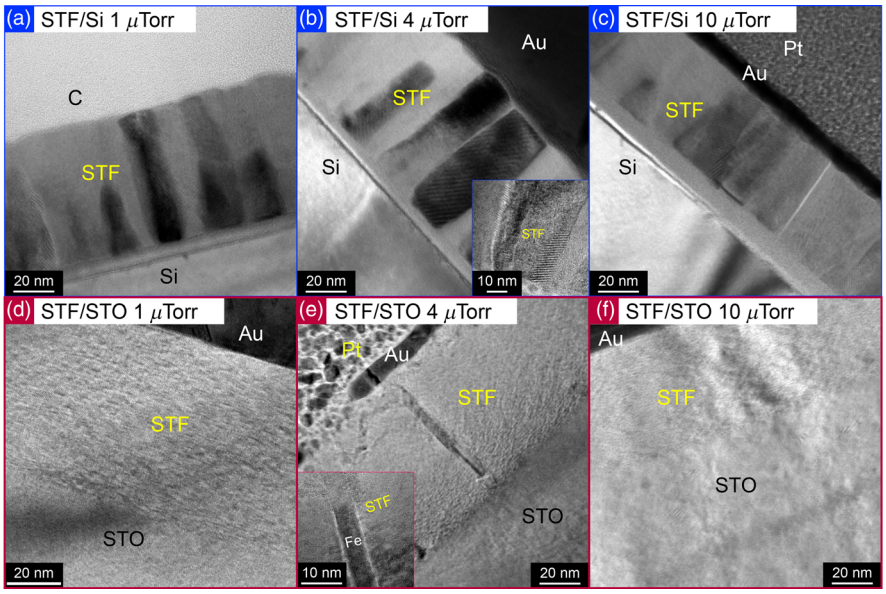

FIG. 2. Transmission electron microscopy of STF samples. Cross-sectional TEM images of STF/Si deposited at $P =$ (a) 1 μTorr, (b) 4 μTorr, and (c) 10 μTorr. Cross-sectional TEM images of STF/STO deposited at $P =$ (d) 1 μTorr, (e) 4 μTorr, showing a Fe rod, and (f) 10 μTorr. Specimens are covered with conductive materials, either Au or C.

et al. and Taguchi *et al.* showed that oxygen vacancies in $SrFeO_{3-\delta}$ and $SrCoO_{3-\delta}$, respectively, increased the unit-cell volume [51,52], and a sufficiently large oxygen deficiency ($\delta > 0.12$) promoted a cubic-to-tetragonal structural change in $SrFeO_{3-\delta}$ [42]. Perry *et al.* showed that the largest lattice parameter is obtained for STF annealed under the most reducing conditions, based on chemical expansion measurements [34]. Chakraverty *et al.* demonstrated that, for $SrFeO_{2.5}$ films on STO grown by PLD, the laser spot size, which affects the growth process, kinetics, and stoichiometry controlled the lattice parameter [53].

C. Film morphology.

Cross-sectional TEM images of STF/Si and STF/STO grown at $P = 1$, 4, and 10 μTorr are given in Fig. 2. All three STF/Si films have a polycrystalline columnar microstructure, and energy-dispersive x-ray spectroscopy (EDX) mapping of the 4-μTorr sample, Fig. 3, indicates a spatial variation in the Fe content, with higher Fe content corresponding to a few of the columnar features. In agreement with the Mössbauer spectroscopy (described below), there is no clear evidence from high-resolution TEM that these columns are metallic Fe, and we presume they represent STF with a higher Fe content than neighboring grains. A similar inhomogeneity is found at $P = 1$ μTorr, but at 10 μTorr the Fe is uniformly distributed. The compound $SrTi_{1-x}Fe_xO_{3-\delta}$ is stable throughout the composition range [13,14], therefore, we assume that the inhomogeneity is different in origin from that seen in spinodal decomposition such as that of Cr-rich (Zn, Cr)Te [54], In-rich (Ga, In)N [55], or (Mn, Ga)As [56] systems. In comparison, the STF grown on STO is single crystal but shows contrast that indicates small-scale structural inhomogeneity, possibly representing layered vacancy ordering as seen in brownmillerite-structured $SrFeO_{2.5}$ [57] and in $(La, Sr)CoO_3$ [58,59].

At $P = 4$ μTorr, a few straight, vertical nanopillars are observed perpendicular to the substrate within the perovskite matrix. Lattice imaging reveals that the pillars are metallic α-Fe. The pillars are sparsely distributed, with spacings of approximately 200 nm in the TEM image of a lamella approximately 20–50 nm thick. This suggests a density of 100–250 pillars per μm^2.

The pillar width is 3–5 nm, giving an estimate of the volume fraction of metallic Fe of 0.1%–0.4%. This volume fraction is small, but it could contribute a significant amount of the net magnetization because metallic Fe has

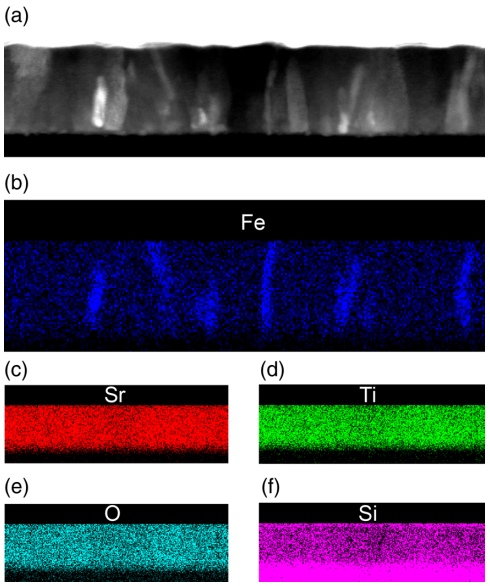

FIG. 3. Composition analysis of STF/Si. (a) STEM images and STEM-EDX element mappings of STF deposited on Si at $P = 4$ μTorr. STEM-EDX element map of (b) Fe, (c) Sr, (d) Ti, (e) O, (f) Si. A Sr peak overlaps the Si peak leading to a false signal for the region of the film in (f).

a high saturation magnetization of 1700 emu cm^{-3}. However, the majority of the Fe remains in the perovskite, e.g., the formation of even 0.5 vol. % metallic Fe would deplete Fe from approximately 8% of the STF volume. Films grown on STO at $P = 1$ and 10 μTorr have no pillars, and the Fe is uniformly distributed.

D. Fe valence state

Measurement of the atomic ratio of Ti and Fe is shown in Fig. 4(a) from energy-dispersive x-ray spectroscopy (EDS, FEI Philips XL 30), confirming that there is no systematic change in the ratio of Fe:Ti (=0.35:0.65) with P.

The Fe valence state is characterized by conversion-electron Mössbauer spectrometry and by x-ray photoelectron spectroscopy (XPS). Conversion-electron Mössbauer spectrometry shows a difference between two films grown at $P = 2$ μTorr on different substrates, as shown in Figs. 4(c) and 4(d). For the STF/Si, a weak paramagnetic signal of Fe^{3+} is detected (approximately 0.7% max emission). The signal may be fitted to a singlet (Gaussian) or, more justifiably (based on Fig. 4(d)), a doublet (2 pseudo-Voigts) as shown in Fig. 4(c), yielding an isomer shift relative to α-Fe of 0.25 ± 0.04 mm s^{-1} and a quadrupole splitting of 0.89 ± 0.08 mm s^{-1}. This signal may arise from Fe^{3+} associated with oxygen vacancies [60]. No other signals are resolved.

The STF/STO shows 0.5%–0.6% emission after optimization. Unlike the sample on Si, the STF/STO shows a metallic iron magnetic phase, identified not just because of the presence of a sextet but also because of the isomer shift of 0.00 ± 0.02 mm s^{-1}, equal to that of α-Fe [Fig. 4(d)]. The peak-intensity ratio of the sextet state indicates that the iron is not uniformly magnetized perpendicular to the substrate [61–63]. There is also a paramagnetic ferric doublet with an isomer shift of 0.35 ± 0.04 mm s^{-1} that accounts for 23% of the peak area. A measurement using Auger electrons sensitive to the top 20–30 nm of the film shows a lower peak-area fraction (15%) for the paramagnetic iron, suggesting a depth dependence of the iron valence state. These results indicate that metallic Fe is present in the STF/STO but not in the STF/Si grown at $P = 2$ μTorr.

Figure 4(b) shows XPS results in which the Fe peaks are similar over the range of deposition pressures and the two substrate types. The peak positions are calibrated so that the Cu peak is present at 284.8 eV. There are no significant differences in the Sr, Ti, and O XPS peaks. The satellite peaks around the Fe $2p_{3/2}$ and $2p_{1/2}$ doublet indicate the presence of Fe^{3+} but not Fe^{2+}, similar to epitaxial $BiFeO_3$ [64] and iron oxides [65]. The lack of a metallic Fe peak in the 4-μTorr sample on STO differs from the TEM results and from the Mössbauer analysis of the $P = 2$ μTorr sample. Since XPS is surface sensitive, we assume that the top parts of the Fe nanorods at the surface would be subject to oxidation, or their very small area coverage may have precluded the observation of a metallic Fe peak.

E. Optical and magnetic characterization

Transmissivity of the films on the two substrates from visible to near-IR wavelengths is shown in Fig. 5. For energies below the band gap, the transmissivity of STF/Si is higher than that of bare silicon because of the antireflection effect that arises from introducing a lower refractive index film on a higher refractive index substrate. The transmissivity of STF/STO and bare STO are similar except for energies just below the band gap where the STF/STO became absorbent.

Atomic force microscope (AFM) images of the STF/Si and STF/STO grown at $P = 4$ μTorr are shown as insets in Fig. 5. The films had a root-mean-square roughness of 1.8 and 2.2 nm, respectively, and have reflective film surfaces. The STF/Si grown at $P = 1$, 4, and 10 μTorr had similar surface topography, with in-plane feature sizes of 20–40 nm. In contrast, the STF/STO grown at $P = 1$

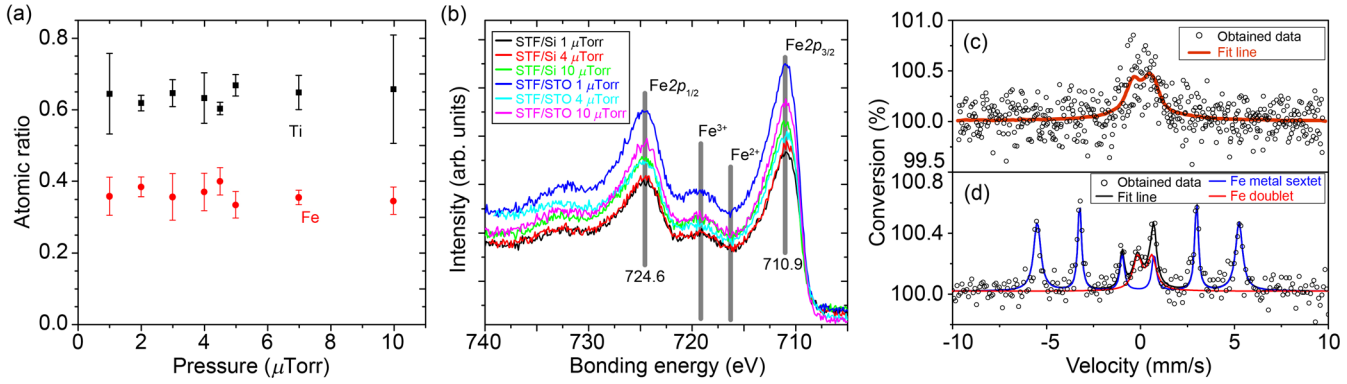

FIG. 4. Composition analysis of the STF films. (a) Atomic ratio of Fe to Ti in STF/STO measured by EDS. Error bars show the standard deviation. (b) XPS peaks from Fe $2p$ in STF films on STO and Si substrates. Mössbauer spectroscopy of (c) STF/Si, and (d) STF/STO, both deposited at $P = 2$ μTorr, measured over the depth of the films. The STF film on the Si substrate does not show the metal sextet phase, but instead, a weak paramagnetic signal.

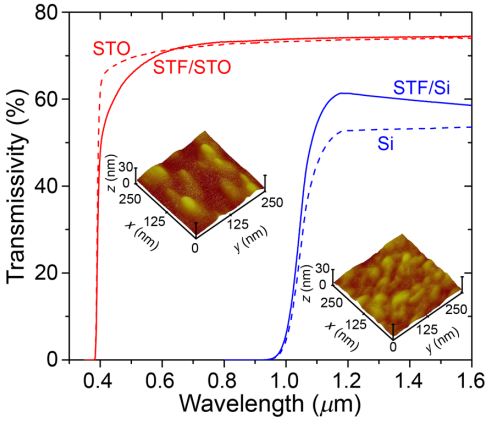

FIG. 5. Optical properties of STF films. Transmission spectra of STF/Si, STF/STO, and their substrates; the insets show the AFM images of the surface topography.

and 10 μTorr is much smoother than the film grown at 4 μTorr.

Figure 6 shows the room-temperature magnetic hysteresis loops from vibrating sample magnetometry (VSM) for films on both substrates as a function of P. Linear substrate signals are subtracted. Uncoated STO substrates subjected to thermal cycling in vacuum in the PLD chamber similar to the thermal cycling during film growth show a diamagnetic response with little change on annealing. For both substrates, the films grown at $P = 4.0$ μTorr show the largest saturation magnetization, while films grown at or above $P = 5$ μTorr do not exhibit a hysteresis loop. The magnetic easy axis is along the out-of-plane direction, with switching fields of 3–4 kOe and a high remanence. The hysteresis loop shape, switching field, and the anisotropy field are generally consistent with those seen in previous studies of STF/STO [16,27,28]. The STF/STO grown at $P = 4$ μTorr has $M_s = 17$ emu cm^{-3}, whereas—remarkably—the

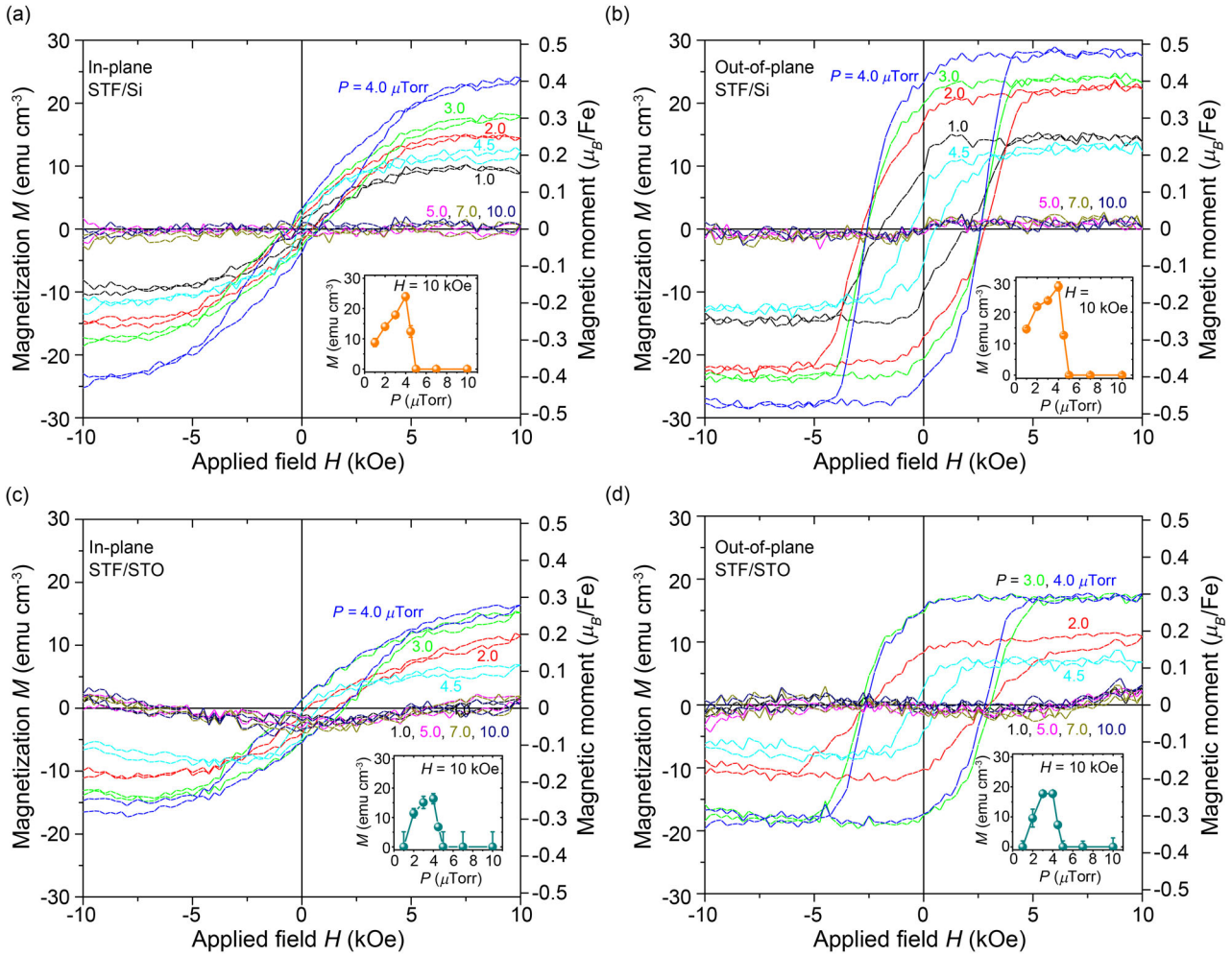

FIG. 6. Magnetic properties of STF films measured by VSM. (a),(b) Magnetic properties of STF/Si specimens. (c),(d) Magnetic properties of STF/STO specimens, (a),(c) in plane and (b),(d) out of plane. Insets show the dependence of the magnetization on pressure at $H = 10$ kOe.

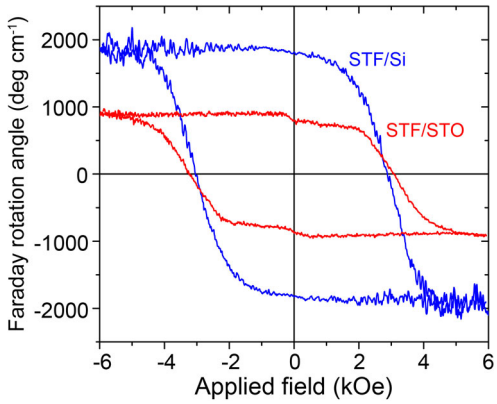

FIG. 7. Magneto-optical properties of STF films. FR loops of STF/Si and STF/STO samples at a wavelength of 1550 nm.

polycrystalline STF/Si has $M_s = 28$ emu cm^{-3}, which is higher by a factor of nearly 2 and corresponds to $0.48\mu_B$/Fe. In the STF/STO, the metallic Fe would contribute approximately 2–6 emu cm^{-3} based on the estimated volume fraction.

The magneto-optical response of STF (FR loop versus applied magnetic field) is measured at a wavelength of 1550 nm by the Faraday-cell-modulation method [66] and is shown in Fig. 7. The field and light are perpendicular to the film in the Faraday measurement, and the Faraday loop shows a comparable shape and coercivity (approximately 3 kOe) to the out-of-plane magnetic hysteresis loops shown in Fig. 6. Low-spin ($S = 1$, $2\mu_B$ per ion) Fe^{4+} can provide splitting of the two circular modes of a linearly polarized optical wave required for FR [29]. The saturation FR angle of STF/Si is approximately 2 times larger than that of STF/STO, reaching $-1900°$ cm^{-1}, i.e., the FR scaled with the saturation magnetization. This FR is approximately 60% of that reported for single-crystal cerium-substituted yttrium iron garnet (CeYIG, $Ce_1Y_2Fe_5O_{12}$) [67,68] at 1550 nm. CeYIG is a candidate material for magneto-optical devices in the near IR. (CeYIG films [4,5,69–71] differ from STF in having an in-plane easy axis.)

F. Discussion

These results illustrate a sensitivity of the STF structure and the optical and magnetic properties to both the pressure during deposition and the substrate type. Both STO and $SrFeO_3$ structures can accommodate significant amounts of oxygen deficiency, maintaining a perovskitelike structure with oxygen vacancies that may be disordered or that can be arranged in layers, e.g., brownmillerite $SrFeO_{2.5}$ when $\delta = 0.5$. The unit-cell volume increases with δ and there are dramatic changes in conductivity and other properties with δ [11,15,20,22–24,72]. Vacancies can even be introduced into an STO substrate at low pressure and high temperature [73], which affects the surface of the substrate prior to film growth.

The oxygen content of the films and, therefore, δ is difficult to quantify because the sample volume is too small for thermogravimetric analysis, although other methods such as photoluminescence, direct imaging, or measurements of cation valence may be applicable [74,75]. However, Rothschild *et al.* [14] showed that Fe^{3+} was the dominant valence state in STF over a range of pressures and temperatures including those corresponding to the growth conditions, i.e., the composition can be written $SrTi_{1-x}Fe_xO_{3-(x/2)-\gamma}$ with γ representing the deviation from a state containing all Fe^{3+}. The presence of Fe^{2+} became significant at extremely low oxygen pressures, e.g., below 10^{-9} Torr at 600 °C, whereas Fe^{4+} was present at higher pressures, e.g., above 10 mTorr. Rodriguez *et al.* showed that a mixture of Fe^{3+} and Fe^{4+} was present in STF after synthesis at 1300 °C in oxygen [76], and Ferreira suggested that some Fe^{4+} was present at room temperature [20]. It is not clear how well the PLD growth conditions correspond to these equilibrium conditions, but we expect that the oxygen content will be kinetically trapped after cooling the samples from the growth temperature, implying that the oxygen content and the average Fe valence state in the films will be lower for films grown at a lower base pressure.

The formation of sparsely distributed metallic Fe nanorods is inferred in the $P = 2$ and 4 μTorr STF/STO samples. This was not seen in our previous work on STF [16], but there have been several other observations of metallic transition metal nanorods forming in an oxide matrix, notably Fe in a (nonperovskite) $LaSrFeO_4$ matrix formed from the deposition of $LaSr_{0.5}Fe_{0.5}O_3$, and Co, Ni, or Fe in ceria or STO by codeposition of the matrix phase with a transition metal oxide [77–79]. In the $P = 4$ μTorr STF/STO, it is possible that the low base pressure combined with the large tetragonal distortion due to epitaxy promotes the precipitation of a fraction of the Fe as a strain relief mechanism that is not seen in the nonepitaxial films on Si. The precipitation of the small volume fraction of metallic Fe would lead to an excess of Sr in the perovskite matrix that could be accommodated through additional SrO layers as in Ruddlesden-Popper phases without disrupting the overall perovskite structure. In contrast, in the films on Si it appears that all the Fe is present within the perovskite lattice. The Fe distribution does, however, become less homogeneous at low base pressure. It is not clear why the STF unit-cell volumes decrease for $P < 4$ μTorr. This may indicate a different strain-relaxation mechanism becoming important, or a structural change due to the ordering of vacancies or the formation of Ti^{3+}.

In previous work, we have suggested that oxygen-deficient STF exhibits mixed valence Fe ions, leading to both ferromagnetic and antiferromagnetic interactions between nearest neighbors. A range of other Fe-based perovskites including Sr_2FeMoO_6 and Ba_2FeReO_6 also display room-temperature magnetism that originates on the

Fe spins [80–82]. Moreover, the magnetic moment of Fe ions is dramatically affected by adjacent oxygen vacancies that break the symmetry of the oxygen coordination octahedron, as predicted theoretically in STCo [83]. Film strain leads to magnetoelastic anisotropy, which can orient the overall direction of magnetization in the film, accounting for the out-of-plane easy axis for STF/STO [16]. The resulting net magnetic moment of the STF and the hysteresis behavior is, therefore, highly dependent on the concentration and arrangement of the oxygen and Fe and the strain state, as well as the presence of Fe nanorods, and is expected to vary with all the film deposition conditions including P. In STCo, changes in P are also found to affect the magnetic moment [22].

The most striking finding in the present work is the higher magnetization and FR in films made on Si compared to those on STO. The films differ in their microstructure and strain state, but may also have subtle differences in oxygen content, vacancy clustering, or Fe distribution despite being deposited simultaneously; this could result from different surface kinetics or surface chemistry during film nucleation, or differing substrate temperatures due to the differences in emissivity and thermal conductivity between the Si and STO substrates. The magnetic effects in STF/Si appear not to originate from metallic Fe, and are, therefore, intrinsic to the substituted perovskite. Metallic behavior has been calculated for STO surfaces [84], suggesting that the grain boundaries in the STF may play a role in its electronic properties. Unlike the STF/STO, which has a significant tetragonal distortion ($c/a > 1$) leading to magnetoelastic anisotropy [27,85], the polycrystalline STF/Si has little strain, suggesting that the origin of its magnetism is microstructural [influenced by grain boundaries, oxygen content, vacancy clustering, or the inhomogeneous Fe distribution observed in Figs. 2(a)–2(c) and 3(b)] rather than magnetoelastic.

III. INTEGRATED MAGNETO-OPTICAL ISOLATOR

The polycrystalline STF/Si is suitable for magneto-optical devices because it is expected to grow on a variety of substrates and it has a large remanent Faraday rotation angle. As an illustration of the integration of polycrystalline STF into a magneto-optical device, a ring resonator is prepared from a silicon-on-insulator wafer consisting of a racetrack placed adjacent to a straight waveguide, similar to the devices shown in Refs. [4,5]. When light passing through the waveguide is resonant with the racetrack (i.e., when the racetrack circumference is an integral number of wavelengths), the light couples into the racetrack, and there is a drop in transmittance through the waveguide, as shown in Fig. 8. If the racetrack is clad on top with a magneto-optical material magnetized perpendicular to the waveguide, the transverse magnetic (TM) mode, but not the transverse electric (TE) mode, experiences a nonreciprocal

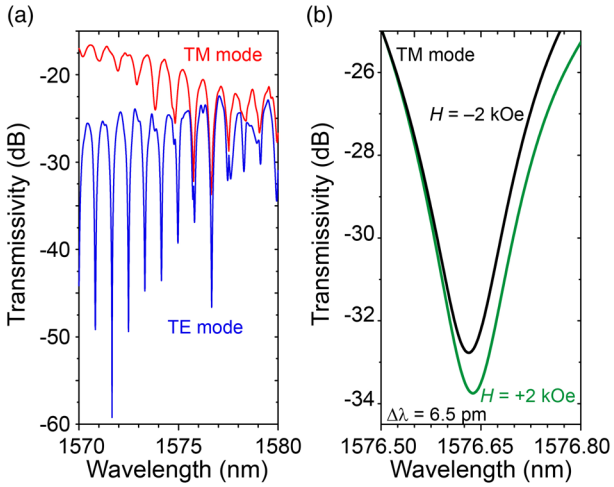

FIG. 8. Integration of STF on a waveguide device. (a) Resonant peaks for TE and TM modes at wavelengths between 1570 and 1580 nm. (b) Example of a peak shift for the TM mode that showed a NRPS of 6.5 nm when the field H direction was reversed.

phase shift (NRPS). This leads to a different resonant wavelength for clockwise and counterclockwise propagating TM light, which forms the basis of an isolator.

The waveguides have a thickness of 250 nm and a width of 450 nm. The racetrack is 290 μm long and 90 μm wide. A 200-μm-long, 20-μm-wide window is opened in the silica cladding of one of the sides of the racetrack and STF (at $P = 4$ μTorr) is deposited over the sample, so that the STF contacted the waveguide directly within the window. The transmittance of the waveguide or resonator is measured at a wavelength of around 1550 nm for a magnetic field of ± 2 kOe applied in plane, perpendicular to the side of the racetrack. The resonant wavelength of both the TM and TE modes varies between successive measurements by up to 10 pm because of thermal drift or vibration, but the TM mode shows an NRPS of approximately 4 pm compared to the TE mode when the sign of the applied field is changed.

Similar devices made with CeYIG cladding [5] (FR $= -1300°$ cm^{-1}) with in-plane magnetization exhibit a NRPS of approximately 20 pm. The lower NRPS in the STF devices is a result of incomplete in-plane saturation, which requires a field >5 kOe. Based on the hysteresis loops, a 2-kOe in-plane field would lead to an in-plane magnetization of approximately 1/3 of the saturation magnetization. The FR scales with the magnetization, so we expect the STF to produce an NRPS of 1/3 of what would be produced at in-plane saturation. The NRPS of the STF devices is in reasonable agreement with the expected NRPS, considering the geometry of the resonator and the magnitude of the FR. The absorption of the STF at a wavelength of $\lambda = 1550$ nm is 31 ± 2 dB cm^{-1}, derived as shown in [70]. Hence, the figure of merit defined as the

ratio of saturation FR to absorption is $58°\,dB^{-1}$, which is good compared with other thin-film magneto-optical materials [17,33].

IV. ELECTRONIC STRUCTURE CALCULATIONS

We now present a brief discussion of the theoretical predictions for the electronic structure and the change of the lattice parameters as a function of the chemical pressure created by oxygen vacancies of STF based on hybrid density functional theory (DFT) [83], as described in the methods section. All possible vacancy and Fe configurations for STF with $x = 0.125$ or 0.25 are evaluated.

From Fig. 9(a), we find that STF with $\delta = 0.125$ and $x = 0.125$ (one Fe atom and one vacancy in the $2 \times 2 \times 2$ perovskite supercell) is a semiconductor with a band gap of approximately 1.1 eV. The e_g orbitals are partially occupied, which gives rise to the ferrimagnetism. From molecular orbital theory, we find that the high-low spin-gap energy is approximately 70 meV, which is actually larger than the approximately 40 meV required to take a spin to the e_g from the t_{2g} level [30]. A detailed analysis of the spin states in this system will be discussed in a subsequent publication.

We confirm the oxidation states are Fe^{2+} and Ti^{4+} rather than both ions being 3+, and the Ti^{4+} magnetic moment is negligible.

When $x = 0.25$, the two Fe ions can be arranged along [001], [110], or [111]. In each case, the Fe-Fe distances are approximately 0.9 times the Ti-Ti distance in STO, and the final unit cell is distorted from cubic symmetry. In the $\delta = 0$ case the Fe ions have an average moment of $3.7\mu_B$, with an antiferromagnetic ground state in the Fe-[001] arrangement. For the [110] and [111] arrangements where the Fe ions are further separated, the lowest energy ferromagnetic (FM) and AF states are almost degenerate within a small energy range <40 meV. The preponderance of [110] and [111] configurations in a crystal with random Fe-site distribution suggests an overall low moment due to dominant AF interactions.

An oxygen vacancy ($\delta = 0.125$) leads to a significant increase in the volume of the unit cell compared to $\delta = 0$, in agreement with experiment. The volume increase is not due to the Fe-Fe interaction but to the chemical pressure created by the vacancy. When calculating the ground state for $\delta = 0.125$, the spin and valence of the two Fe ions are initialized in all possible combinations (i.e., both Fe^{3+}, one

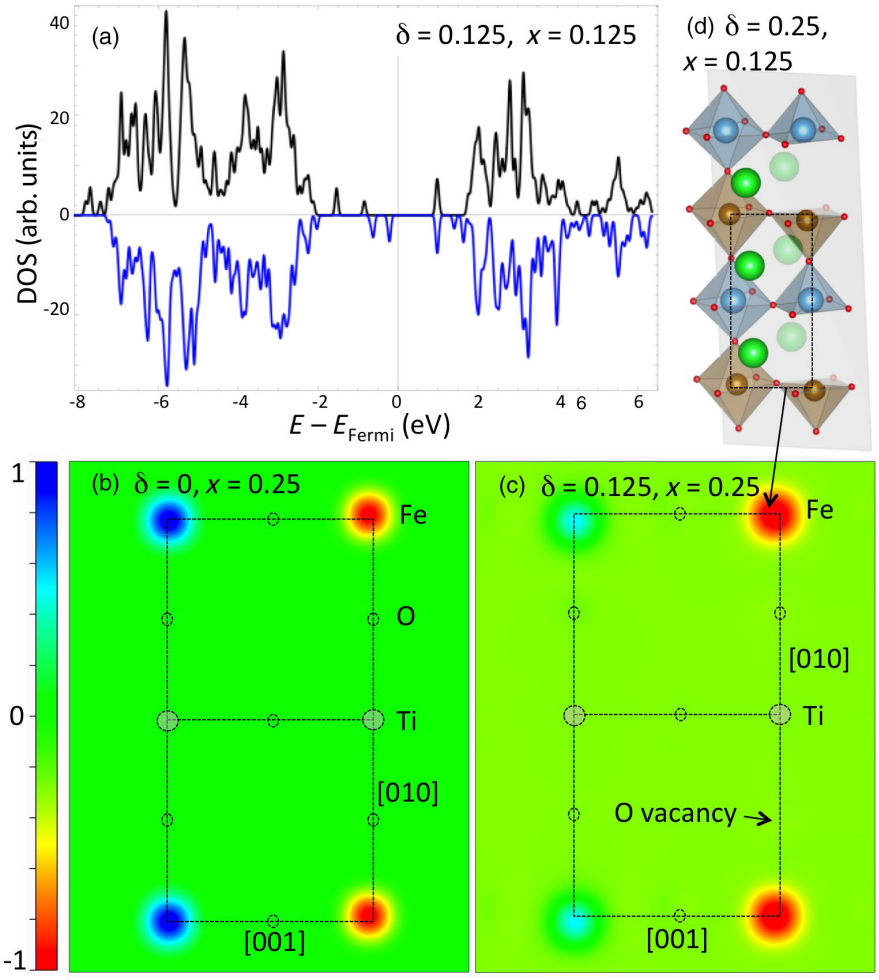

FIG. 9. DFT calculations. (a) Total density of states for $SrTi_{0.875}Fe_{0.125}O_{2.875}$ (high spin Fe) obtained with HSE06. The supercell contains one Fe ion and one neighboring vacancy. (b) Spin density (HSE) projected onto the (100) plane for $SrTi_{0.75}Fe_{0.25}O_3$ in which the two nearest-neighbor Fe ions are aligned in the [001] direction, showing clearly their antiferromagnetic ordering. (c) Spin density (HSE) projected onto the (100) plane for $SrTi_{0.75}Fe_{0.25}O_{2.875}$ with an oxygen vacancy adjacent to one of the two Fe ions per unit cell. In both cases (b) and (c), the second-nearest Fe neighbors are also depicted and the color scale indicates the spin density normalized to the largest magnetic moment. The ferrimagnetic order in the O-deficient system is clear in (c). (d) Image showing the model in (c) in which the atomic positions are visible. The plane shown in (c) bisects the model passing through the Fe and Ti sites. Blue, Ti; brown, Fe; green, Sr; red, O.

Fe^{4+} and one Fe^{2+}, high and low spin, and FM and AF) and the lowest energy state after relaxation is defined as the ground state. The low-spin states tend to shift to high spin with approximately 4.1–4.2μ_B, with the two Fe spins coupled AF in most but not all cases. However, even the AF-initialized cells have a net moment, i.e., they are ferrimagnetic, because the spin at each Fe location is not identical owing to their different locations with respect to the oxygen vacancy.

In the Fe-[001] case, the lowest energy configuration is one where the vacancy is between the two Fe ions, which eliminates the superexchange between the Fe ions that coordinate the vacancy. The magnetic moment is approximately 0.2μ_B/Fe. In the Fe-[110] case, the two possible vacancy positions lead to similar energies, and the magnetization in the ground state is 0.3–0.4μ_B/Fe. In the more symmetric case of Fe-[111], the FM and AF configurations are almost degenerate (i.e., <0.1 meV) because of the large separation between the Fe atoms. The final magnetic moment of the AF-initialized arrangement is once again 0.1–0.2μ_B/Fe.

To better understand the effects of the vacancies on the magnetic behavior, we calculate the HSE spin density for a system with $x = 0.25$ and $\delta = 0$ or $\delta = 0.125$. Figure 9(b) shows the spin density projected onto the (100) plane for $SrTi_{0.75}Fe_{0.25}O_3$ in which the two Fe ions are aligned in the [001] direction. The AF ordering of the two Fe ions is seen from the opposite sign but equal value of the spin density. In Fig. 9(c), a vacancy is introduced, i.e., the composition is $SrTi_{0.75}Fe_{0.25}O_{2.875}$ with the vacancy placed adjacent to one Fe ion but not between the two Fe ions. The magnetic moment of the Fe next to the vacancy is enhanced, as is evident by the slightly larger radius of the red spin-density projections, while the other Fe which is completely O coordinated has a smaller magnetic moment (blue) coupled antiferrimagnetically to the larger moment of the first Fe. While the two Fe magnetic moments per unit cell in the first case are equal in magnitude, in the O-coordinated Fe case there is a difference of 0.1–0.3μ_B/Fe between the moments (i.e., the system is ferrimagnetic), in accordance with our previous discussion. These results have been qualitatively confirmed using LMTO (linear muffin-tin orbital). In the case of Fig. 9(c) the magnetic moment of the incompletely coordinated Fe is higher, and this is the case for most of the possible combinations of Fe valence and spin state. However, a few configurations with a slightly higher energy show an increase of the moment of both Fe ions or even an increase just of the magnetic moment of the completely coordinated Fe ion.

The STF film is expected to comprise randomly distributed Fe ions and vacancies, and we would, therefore, expect a variety of nearest-neighbor configurations and resulting interactions to be present, including those addressed in the modeling. The crystal would then exhibit a relatively low net magnetic moment, dominated by AF coupling, analogous to a ferrimagnet but without long-range order. The presence of vacancies is predicted to increase the unit-cell volume, raise the magnetic moment at the Fe sites, and to lead to a net moment even when AF interactions are dominant. These predictions are broadly in line with the experimental results.

V. CONCLUSION

In conclusion, STF ($SrTi_{0.65}Fe_{0.35}O_{3-\delta}$) films grown on Si or STO substrates by PLD show a strong dependence of microstructure and magnetic properties on the base pressure during deposition. At an optimum base pressure for deposition ($P = 4$ μTorr) the films show room-temperature magnetism of up to 0.53μ_B/Fe with out-of-plane magnetic anisotropy, and a coercivity of 3 kOe as well as a FR of $-1900°$ cm^{-1} at a wavelength of 1550 nm. STF grown on STO at the optimum base pressure of $P =$ 4 μTorr shows a low (<0.5%) volume fraction of metallic Fe nanorods not present at other pressures that contribute to the magnetic signal, but the polycrystalline STF films grown on Si show 65% greater magnetization and FR compared to the epitaxial films on STO. There is no evidence of metallic Fe in the STF/Si, indicating that the magnetic and magneto-optical properties are intrinsic to the substituted perovskite. Polycrystalline STF is grown onto a silicon ring resonator, and its FR produces a nonreciprocal phase shift. First-principles calculations show that oxygen vacancies increase both the unit-cell volume and the magnetic moment of the Fe ions. The dominant interactions are antiferromagnetic, leading to a material with a net magnetization below about 0.5μ_B/Fe, which is reasonable compared with the experimental data. These results illustrate the important role of oxygen vacancies in determining the magnetic properties and structure of a Fe-substituted perovskite, and the integration of the perovskite in magneto-optical devices.

ACKNOWLEDGMENTS

T. G. acknowledges support from the JST PRESTO, JSPS Postdoctoral Fellowships for Research Abroad, Grant-in-Aid for Young Scientists (A) No. 26706009, and Challenging Exploratory Research No. 26600043. C. R. acknowledges support from the NSF DMR1419807 and ECCS1607865 and from FAME, a SRC STARnet Center supported by DARPA and MARCO. H. L. T. acknowledges support from the NSF DMR1419807. P. V. acknowledges support from the Center for Development of Nanoscience and Nanotechnology, CEDENNA, Chile. J. M. F. acknowledges support from Fondecyt Iniciación 11130128 and DGIIP USM, Chile. M. I. acknowledges support from the JSPS Grant-in-Aid for Scientific Research (S) No. 26220902. This work utilized the shared experimental facilities of the Center for Materials Science and Engineering (CMSE), Award

No. NSF DMR1419807. We thank Professor Lei Bi (University of Electronic Science and Technology of China), Dr. Vivek Singh (MIT), Professor Lionel C. Kimerling (MIT), and Mr. Masahiko Watanabe (Elionix) for experimental support and discussions.

APPENDIX A: TARGET PREPARATION

$SrCO_3$ (99.99%), TiO_2 (99.99%), and Fe_2O_3 (hematite, 99.945%) powders are stoichiometrically mixed, ball milled for 24 h, and calcined at 1200 °C for 5 h, showing a single perovskite phase. The powder is pressed into a 1-inch-diameter pellet and sintered at 1300 °C for 5 h.

APPENDIX B: SAMPLE PREPARATION FOR TEM

The samples are prepared using a focused ion beam (FEI-600), and then imaged on a JEOL 2010F field emission TEM at a 200-kV acceleration voltage. The element distribution in the sample is mapped by STEM EDX.

APPENDIX C: X-RAY DIFFRACTION

For STF/STO, the PANAlytical X'pert is used. The wavelength is Cu-Kα ($\lambda = 1.540\,598$ Å), the source current is 40 mA, the voltage is 45 kV, and the scan step in 2θ is 0.017°. There is no offset of ω. For STF/STO reciprocal space maps, the Bruker-AXS D8 DISCOVER is used with Cu-Kα radiation. The x-ray beam is monochromated with the Ge(220) × 4, and the Gobel mirror slit is 0.8 mm. The first and second monochromator slits are 0.2 and 1 mm. For STF/Si, the Rigaku Smartlab is used because of its capability for in-plane grazing-incidence diffraction. The wavelength is Cu-Kα with a tube current of 200 mA and a voltage of 45 kV. The step of the 2θ goniometer is 0.024°, and the incident angle of the x rays ω is fixed at 0.4°.

APPENDIX D: MÖSSBAUER SPECTROSCOPY

^{57}He Mössbauer spectroscopy with a ^{57}Co/Rh source (of approximately 20 mCi of activity) is performed at 300 K in order to characterize the iron in the samples using the conversion-electron mode. The films are first metallized with a thin layer of aluminum (approximately 30–40 nm) to provide a good Ohmic contact and subsequently inserted into the cathode structure of a He-CH_4 filled (5% at 1.7 bar) gas-flow proportional counter, for measurements lasting approximately one week in each case. Energy-filtering-enabled Mössbauer spectra are acquired for the film (deep electrons and x-rays) and primarily from the surface (approximately 20–30 nm penetration depth, due to Auger electrons) for the sample on STO. No Mössbauer signal can be resolved for the lowest escape energies. The sample on Si has a weaker signal and no energy filtering is performed, so the data correspond to the full thickness. The spectra are fitted using the standard least-squares method, using a pure Fe metal foil for velocity calibration.

APPENDIX E: THEORETICAL METHOD

We perform spin-polarized DFT calculations with a Heyd-Scuseria-Ernzerhof (HSE) functional [86,87] as implemented in the Vienna *ab initio* simulation package and within a projector-augmented-wave–Perdew-Burke-Ernzerhof framework [88]. Compared to semilocal DFT methods, HSE improves the accuracy of standard local magnetic moments as well as features of interest such as valence spin states, band gaps, and lattice parameters, as shown previously for $SrCoO_3$ and $SrTiCoO_3$ [83]. A $2 \times 2 \times 2$ perovskite supercell with 39 or 40 atoms for $\delta = 0$ or 0.125, respectively, is used. Monkhorst k-point meshes of $2 \times 2 \times 2$ and $4 \times 4 \times 4$ are used for relaxation and static calculations, respectively. The energy cutoff used is 500 eV, and forces are converged to within 10^{-5} eV Å^{-1}.

We explore all possible FM and AFM initializations in both high- and low-spin configurations for different combinations of valence states for Fe, i.e., $4\mu_B$ and $0\mu_B$ (high- and low-spin Fe^{2+}), $5\mu_B$ and $1\mu_B$ (high- and low-spin Fe^{3+}), and $4\mu_B$ and $2\mu_B$ (high- and low-spin Fe^{4+}). We also explore perturbations of $\pm 20\%\mu_B$ for every initialization. In total, a few hundred calculations are performed, and in all cases, the magnetic moments are allowed to fully relax to their final value. Some cases with $4 \times 4 \times 4$ supercells are also examined with $x = 0.25$ and $\delta = 0.125$, of which a few reach convergence within a reasonable time. These configurations show antiferromagnetic coupling between the Fe moments and agree with the $2 \times 2 \times 2$ supercell results.

[1] J. Wang, J. B. Neaton, H. Zheng, V. Nagarajan, S. B. Ogale, B. Liu, D. Viehland, V. Vaithyanathan, D. G. Schlom, U. V. Waghmare, N. A. Spaldin, K. M. Rabe, M. Wuttig, and R. Ramesh, Epitaxial $BiFeO_3$ multiferroic thin film heterostructures, Science **299**, 1719 (2003).

[2] G. Rijnders and D. H. A. Blank, Materials science: Build your own superlattice, Nature (London) **433**, 369 (2005).

[3] A. Gozar, G. Logvenov, L. F. Kourkoutis, A. T. Bollinger, L. A. Giannuzzi, D. A. Muller, and I. Bozovic, High-temperature interface superconductivity between metallic and insulating copper oxides, Nature (London) **455**, 782 (2008).

[4] L. Bi, J. Hu, P. Jiang, D. H. Kim, G. F. Dionne, L. C. Kimerling, and C. A. Ross, On-chip optical isolation in monolithically integrated non-reciprocal optical resonators, Nat. Photonics **5**, 758 (2011).

[5] T. Goto, M. C. Onbasli, D. H. Kim, V. Singh, M. Inoue, L. C. Kimerling, and C. A. Ross, A nonreciprocal racetrack resonator based on vacuum-annealed magnetooptical cerium-substituted yttrium iron garnet, Opt. Express **22**, 19047 (2014).

[6] G. M. Choi, H. L. Tuller, and D. Goldschmidt, Electronic-transport behavior in single-crystalline$Ba_{0.03}Sr_{0.97}TiO_3$, Phys. Rev. B **34**, 6972 (1986).

[7] J. H. Haeni, P. Irvin, W. Chang, R. Uecker, P. Reiche, Y. L. Li, S. Choudhury, W. Tian, M. E. Hawley, B. Craigo, A. K. Tagantsev, X. Q. Pan, S. K. Streiffer, L. Q. Chen, S. W. Kirchoefer, J. Levy, and D. G. Schlom, Room-temperature ferroelectricity in strained $SrTiO_3$, Nature (London) **430**, 758 (2004).

[8] A. Ohtomo and H. Y. Hwang, A high-mobility electron gas at the $LaAlO_3/SrTiO_3$ heterointerface, Nature (London) **427**, 423 (2004).

[9] A. D. Caviglia, S. Gariglio, N. Reyren, D. Jaccard, T. Schneider, M. Gabay, S. Thiel, G. Hammerl, J. Mannhart, and J. M. Triscone, Electric field control of the $LaAlO_3/SrTiO_3$ interface ground state, Nature (London) **456**, 624 (2008).

[10] K. Ueno, S. Nakamura, H. Shimotani, A. Ohtomo, N. Kimura, T. Nojima, H. Aoki, Y. Iwasa, and M. Kawasaki, Electric-field-induced superconductivity in an insulator, Nat. Mater. **7**, 855 (2008).

[11] W. Jung and H. L. Tuller, Impedance study of $SrTi_{1-x}Fe_xO_{3-\delta}$ ($x = 0.05$ to 0.80) mixed ionic-electronic conducting model cathode, Solid State Ionics **180**, 843 (2009).

[12] W. Jung and H. L. Tuller, Investigation of cathode behavior of model think-film $SrTi_{1-x}FexO_{3-\delta}$ (x = 0.35 and 0.5) mixed ionic-electronic conducting electrodes, J. Electrochem. Soc. **155**, B1194 (2008).

[13] L. H. Brixner, Preparation and properties of the $SrTi_{1-x}Fe_xO_{3-x/2}O_{x/2}$ system, Mater. Res. Bull. **3**, 299 (1968).

[14] A. Rothschild, W. Menesklou, H. L. Tuller, and E. Ivers-Tiffée, Electronic structure, defect chemistry, and transport properties of $SrTi_{1-x}Fe_xO_{3-y}$ solid solutions, Chem. Mater. **18**, 3651 (2006).

[15] D. P. Fagg, V. V. Kharton, A. V. Kovalevsky, A. P. Viskup, E. N. Naumovich, and J. R. Frade, The stability and mixed conductivity in La and Fe doped $SrTiO_3$ in the search for potential SOFC anode materials, J. Eur. Ceram. Soc. **21**, 1831 (2001).

[16] D. H. Kim, L. Bi, P. Jiang, G. F. Dionne, and C. A. Ross, Magnetoelastic effects in $SrTi_{1-x}M_xO_3$ (M = Fe, Co, or Cr) epitaxial thin films, Phys. Rev. B **84**, 014416 (2011).

[17] H.-S. Kim, L. Bi, G. F. Dionne, and C. A. Ross, Magnetic and magneto-optical properties of Fe-doped $SrTiO_3$ films, Appl. Phys. Lett. **93**, 092506 (2008).

[18] Y. G. Wang, X. G. Tang, Q. X. Liu, Y. P. Jiang, and Z. Y. Feng, Ferroelectric and ferromagnetic properties of $SrTi_{0.9}Fe_{0.1}O_{3-\delta}$ thin films, Solid State Commun. **202**, 24 (2015).

[19] H.-S. Kim, L. Bi, D. H. Kim, D.-J. Yang, Y. J. Choi, J. W. Lee, J. K. Kang, Y. Chang Park, G. F. Dionne, and C. A. Ross, Ferromagnetism in single crystal and nanocomposite $Sr(Ti, Fe)O_3$ epitaxial films, J. Mater. Chem. **21**, 10364 (2011).

[20] A. A. L. Ferreira, J. C. C. Abrantes, J. R. Jurado, and J. R. Frade, Oxygen stoichiometry of $Sr_{0.97}(Ti, Fe)O_{3-\delta}$ materials, Solid State Ionics **135**, 761 (2000).

[21] M. Kuhn, J. J. Kim, S. R. Bishop, and H. L. Tuller, Oxygen nonstoichiometry and defect chemistry of perovskite-structured $Ba_xSr_{1-x}Ti_{1-y}Fe_yO_{3-y/2+\delta}$ solid solutions, Chem. Mater. **25**, 2970 (2013).

[22] S. Steinsvik, R. Bugge, J. O. N. Gjønnes, J. Taftø, and T. Norby, The defect structure of $SrTi_{1-X}Fe_xO_{3-Y}$ ($x = 0$–0.8) investigated by electrical conductivity measurements and electron energy loss spectroscopy (EELS), J. Phys. Chem. Solids **58**, 969 (1997).

[23] V. V. Kharton, A. V. Kovalevsky, A. P. Viskup, F. M. Figueiredo, J. R. Frade, A. A. Yaremchenko, and E. N. Naumovich, Faradaic efficiency and oxygen permeability of $Sr_{0.97}Ti_{0.6}Fe_{0.4}O_{3-\delta}$ perovskite, Solid State Ionics **128**, 117 (2000).

[24] J. R. Jurado, F. M. Figueiredo, B. Gharbage, and J. R. Frade, Electrochemical permeability of $Sr_{0.7}(Ti, Fe)O_{3-\delta}$ materials, Solid State Ionics **118**, 89 (1999).

[25] L. A. Errico, M. Rentería, and M. Weissmann, Theoretical study of magnetism in transition-metal-doped TiO_2 and $TiO_{2-\delta}$, Phys. Rev. B **72**, 184425 (2005).

[26] L. Bi, H.-S. Kim, G. F. Dionne, and C. A. Ross, Structure, magnetic properties and magnetoelastic anisotropy in epitaxial $Sr(Ti_{1-x}Co_x)O_3$ films, New J. Phys. **12**, 043044 (2010).

[27] D. H. Kim, N. M. Aimon, L. Bi, G. F. Dionne, and C. A. Ross, The role of deposition conditions on the structure and magnetic properties of $SrTi_{1-x}Fe_xO_3$ films, J. Appl. Phys. **111**, 07A918 (2012).

[28] D. H. Kim, N. M. Aimon, L. Bi, J. M. Florez, G. F. Dionne, and C. A. Ross, Magnetostriction in epitaxial $SrTi_{1-x}Fe_xO_{3-\delta}$ perovskite films with $x = 0.13$ and 0.35, J. Phys. Condens. Matter **25**, 026002 (2013).

[29] G. F. Dionne, *Magnetic Oxides* (Springer, Berlin, Heidelberg, New York, 2009).

[30] G. F. Dionne, Evidence of magnetoelastic spin ordering in dilute magnetic oxides, J. Appl. Phys. **101**, 09C509 (2007).

[31] H.-S. Kim, L. Bi, H. Paik, D.-J. Yang, Y. C. Park, G. F. Dionne, and C. A. Ross, Self-assembled single-phase perovskite nanocomposite thin films, Nano Lett. **10**, 597 (2010).

[32] M. Shone, The technology of YIG film growth, Circuits Syst. Signal Process. **4**, 89 (1985).

[33] M. C. Onbaşl\imath, T. Goto, A. Tang, A. Pan, E. Battal, A. K. Okyay, G. F. Dionne, and C. A. Ross, Oxygen partial pressure dependence of magnetic, optical and magneto-optical properties of epitaxial cobalt-substituted $SrTiO_3$ films, Opt. Express **23**, 13399 (2015).

[34] N. H. Perry, J. J. Kim, S. R. Bishop, and H. L. Tuller, Strongly coupled thermal and chemical expansion in the perovskite oxide system $Sr(Ti, Fe)O_{3-\alpha}$, J. Mater. Chem. A **3**, 3602 (2015).

[35] T. Goto, A. V. Baryshev, K. Tobinaga, and M. Inoue, Faraday rotation of a magnetophotonic crystal with the dual-cavity structure, J. Appl. Phys. **107**, 09A946 (2010).

[36] T. Goto, A. V. Dorofeenko, A. M. Merzlikin, A. V. Baryshev, A. P. Vinogradov, M. Inoue, A. A. Lisyansky, and A. B. Granovsky, Optical Tamm States in One-Dimensional Magnetophotonic Structures, Phys. Rev. Lett. **101**, 113902 (2008).

[37] M. Levy, R. M. Osgood, Jr., H. Hegde, F. J. Cadieu, R. Wolfe, and V. J. Fratello, Integrated optical isolators with sputter-deposited thin-film magnets, IEEE Photonics Technol. Lett. **8**, 903 (1996).
[38] M. C. Onbasli, T. Goto, X. Sun, N. Huynh, and C. A. Ross, Integration of bulk-quality thin film magneto-optical cerium-doped yttrium iron garnet on silicon nitride photonic substrates, Opt. Express **22**, 25183 (2014).
[39] I. L. Lyubchanskii, N. N. Dadoenkova, M. I. Lyubchanskii, E. A. Shapovalov, A. E. Zabolotin, Y. P. Lee, and T. Rasing, Response of two-defect magnetic photonic crystals to oblique incidence of light: Effect of defect layer variation, J. Appl. Phys. **100**, 096110 (2006).
[40] T. Goto, R. Isogai, and M. Inoue, Para-magneto- and electro-optic microcavities for blue wavelength modulation, Opt. Express **21**, 19648 (2013).
[41] T. Goto, R. Hashimoto, R. Isogai, Y. Suzuki, R. Araki, H. Takagi, and M. Inoue, Fabrication of microcavity with magneto- and electro-optical film, J. Magn. Soc. Jpn. **36**, 197 (2012).
[42] M. Inoue, M. Levy, and A. V. Baryshev, *Magnetophotonics from Theory to Applications* (Springer, Berlin, Heidelberg, New York, 2014).
[43] G. Fan, K. Pennington, and J. H. Greiner, Magneto-Optic Hologram, J. Appl. Phys. **40**, 974 (1969).
[44] R. Isogai, S. Suzuki, K. Nakamura, Y. Nakamura, H. Takagi, T. Goto, P. B. Lim, and M. Inoue, Collinear volumetric magnetic holography with magnetophotonic microcavities, Opt. Express **23**, 13153 (2015).
[45] H.-Y. S. Li and D. Psaltis, Three-dimensional holographic disks, Appl. Opt. **33**, 3764 (1994).
[46] H. J. Coufal, D. Psaltis, and G. T. Sincerbox, *Holographic Data Storage* (Springer, New York, 2000).
[47] L. Bi, J. Hu, G. F. Dionne, L. Kimerling, and C. A. Ross, in Integrated Optics: Devices, Materials, and Technologies XV, edited by J. E. Broquin and G. N. Conti, *SPIE Proceedings Vol. 7941* (SPIE, San Francisco, California, USA, 2011), p. 5.
[48] H. E. Swanson, G. M. Ugrinic, R. K. Fuyat, and S. United, *Standard X-Ray Diffraction Powder Patterns* (National Bureau of Standards, Washington, DC, 1954), Vol. III, p. 44.
[49] I. D. Zhitomirskii, O. I. Chechernikova, V. V. Ivanova, and Y. N. Venevtsev, $(Pb_xSr_{1-x})(Fe_{2/3}Te_{1/3})O_3$ and $Sr[Fe_{2/3}(Te_xW_{1-x})_{1/3}]O_3$ solid solutions, Inorg. Mater. (USSR) **19**, 849 (1983).
[50] T. Ohnishi, K. Shibuya, T. Yamamoto, and M. Lippmaa, Defects and transport in complex oxide thin films, J. Appl. Phys. **103**, 103703 (2008).
[51] J. B. MacChesney, R. C. Sherwood, and J. F. Potter, Electric and magnetic properties of the strontium ferrates, J. Chem. Phys. **43**, 1907 (1965).
[52] H. Taguchi, M. Shimada, and M. Koizumi, The effect of oxygen vacancy on the magnetic properties in the system $SrCoO_{3-\delta}$ $(0 < \delta < 0.5)$, J. Solid State Chem. **29**, 221 (1979).
[53] S. Chakraverty, A. Ohtomo, M. Okude, K. Ueno, and M. Kawasaki, Epitaxial structure of (001)- and (111)-oriented perovskite ferrate films grown by pulsed-laser deposition, Cryst. Growth Des. **10**, 1725 (2010).
[54] S. Kuroda, N. Nishizawa, K. Takita, M. Mitome, Y. Bando, K. Osuch, and T. Dietl, Origin and control of high-temperature ferromagnetism in semiconductors, Nat. Mater. **6**, 440 (2007).
[55] T. Dietl, From our readers: Self-organized growth controlled by charge states of magnetic impurities, Nat. Mater. **5**, 673 (2006).
[56] M. Yokoyama, H. Yamaguchi, T. Ogawa, and M. Tanaka, Zinc-blende-type MnAs nanoclusters embedded in GaAs, J. Appl. Phys. **97**, 10D317 (2005).
[57] Y. Shimakawa, S. Inoue, M. Haruta, M. Kawai, K. Matsumoto, A. Sakaiguchi, N. Ichikawa, S. Isoda, and H. Kurata, Topotactic changes in thin films of brownmillerite $SrFeO_{2.5}$ grown on $SrTiO_3$ substrates to infinite-layer structure $SrFeO_2$, Cryst. Growth Des. **10**, 4713 (2010).
[58] M. Sharma, J. Gazquez, M. Varela, J. Schmitt, and C. Leighton, Growth temperature control of the epitaxy, magnetism, and transport in $SrTiO_3(001)/La_{0.5}Sr_{0.5}CoO_3$ thin films, J. Vac. Sci. Technol. A **29**, 051511 (2011).
[59] J. Gazquez, S. Bose, M. Sharma, M. A. Torija, S. J. Pennycook, C. Leighton, and M. Varela, Lattice mismatch accommodation via oxygen vacancy ordering in epitaxial $La_{0.5}Sr_{0.5}CoO_{3-\delta}$ thin films, APL Mater. **1**, 012105 (2013).
[60] T. C. Gibb, P. D. Battle, S. K. Bollen, and R. J. Whitehead, Investigation of the crystal and magnetic structure of the perovskite system Sr_2FeTiO_{6-y} by Mössbauer spectroscopy and neutron diffraction, J. Mater. Chem. **2**, 111 (1992).
[61] U. Gonser, *Mössbauer Spectroscopy* (Springer, Berlin, Heidelberg, 1975).
[62] U. Gonser, *Microscopic Methods in Metals* (Springer, Berlin, Heidelberg, 1986).
[63] F. E. Fujita, *Physics of New Materials* (Springer, Berlin, Heidelberg, 1998).
[64] W. Eerenstein, F. D. Morrison, J. Dho, M. G. Blamire, J. F. Scott, and N. D. Mathur, Comment on "Epitaxial $BiFeO_3$ multiferroic thin film heterostructures," Science **307**, 1203 (2005).
[65] T. Schedel-Niedrig, W. Weiss, and R. Schlögl, Electronic structure of ultrathin ordered iron oxide films grown onto Pt(111), Phys. Rev. B **52**, 17449 (1995).
[66] K. Sato, Hikari-to-jiki (Asakura-shoten, Tokyo, 2007), p. 92.
[67] T. Shintaku, A. Tate, and S. Mino, Ce-substituted yttrium iron garnet films prepared on $Gd_3Sc_2Ga_3O_{12}$ garnet substrates by sputter epitaxy, Appl. Phys. Lett. **71**, 1640 (1997).
[68] S. Higuchi, Y. Furukawa, S. Takekawa, O. Kamada, K. Kitamura, and K. Uyeda, Magnetooptical properties of cerium-substituted yttrium iron garnet single crystals for magnetic-field sensor, Sens. Actuators A **105**, 293 (2003).
[69] B. Stadler, K. Vaccaro, P. Yip, J. Lorenzo, L. Yi-Qun, and M. Cherif, Integration of magneto-optical garnet films by metal-organic chemical vapor deposition, IEEE Trans. Magn. **38**, 1564 (2002).
[70] T. Goto, Y. Eto, K. Kobayashi, Y. Haga, M. Inoue, and C. A. Ross, Vacuum annealed cerium-substituted yttrium iron garnet films on non-garnet substrates for integrated optical circuits, J. Appl. Phys. **113**, 17A939 (2013).
[71] T. Goto, M. C. Onbasli, and C. A. Ross, Magneto-optical properties of cerium substituted yttrium iron garnet films

with reduced thermal budget for monolithic photonic integrated circuits, Opt. Express **20**, 28507 (2012).
[72] C. Greaves and R. A. Buker, The defect structure of Sr_2FeTiO_{6-x}, Mater. Res. Bull. **21**, 823 (1986).
[73] C. Yu, M. L. Scullin, M. Huijben, R. Ramesh, and A. Majumdar, The influence of oxygen deficiency on the thermoelectric properties of strontium titanates, Appl. Phys. Lett. **92**, 092118 (2008).
[74] D. A. Muller, N. Nakagawa, A. Ohtomo, J. L. Grazul, and H. Y. Hwang, Atomic-scale imaging of nanoengineered oxygen vacancy profiles in $SrTiO_3$, Nature (London) **430**, 657 (2004).
[75] M. A. A. Franco and M. V. Regi, Anion deficiency in strontium titanate, Nature (London) **270**, 706 (1977).
[76] J. Rodriguez, J. A. Pereda, M. Vallet, J. G. Calbet, and J. Tejada, Mössbauer study of vacancy ordering in the system $SrTi_{1-x}Fe_xO_{3-y}$ $(0.50 \leq x \leq 0.70)$, Mater. Res. Bull. **21**, 255 (1986).
[77] F. Vidal, Y. Zheng, J. Milano, D. Demaille, P. Schio, E. Fonda, and B. Vodungbo, Nanowires formation and the origin of ferromagnetism in a diluted magnetic oxide, Appl. Phys. Lett. **95**, 152510 (2009).
[78] P. Schio, F. Vidal, Y. Zheng, J. Milano, E. Fonda, D. Demaille, B. Vodungbo, J. Varalda, A. J. A. de Oliveira, and V. H. Etgens, Magnetic response of cobalt nanowires with diameter below 5 nm, Phys. Rev. B **82**, 094436 (2010).
[79] F. Vidal, P. Schio, N. Keller, Y. Zheng, D. Demaille, F. J. Bonilla, J. Milano, and A. J. A. de Oliveira, Magneto-optical study of slanted Co nanowires embedded in CeO_2/$SrTiO_3(0\,0\,1)$, Physica (Amsterdam) **407B**, 3070 (2012).
[80] A. W. Sleight and J. F. Weiher, Magnetic and electrical properties of Ba_2MReO_6 ordered perovskites, J. Phys. Chem. Solids **33**, 679 (1972).
[81] T. Nakagawa, Magnetic and electrical properties of ordered perovskite $Sr_2(FeMo)O_6$ and its related compounds, J. Phys. Soc. Jpn. **24**, 806 (1968).
[82] B. García-Landa, C. Ritter, M. R. Ibarra, J. Blasco, P. A. Algarabel, R. Mahendiran, and J. García, Magnetic and magnetotransport properties of the ordered perovskite Sr_2FeMoO_6, Solid State Commun. **110**, 435 (1999).
[83] J. M. Florez, S. P. Ong, M. C. Onbaşli, G. F. Dionne, P. Vargas, G. Ceder, and C. A. Ross, First-principles insights on the magnetism of cubic $SrTi_{1-x}Co_xO_{3-\delta}$, Appl. Phys. Lett. **100**, 252904 (2012).
[84] A. R. Silva and G. M. Dalpian, Oxygen vacancies at the surface of $SrTiO_3$ thin films, J. Appl. Phys. **115**, 033710 (2014).
[85] P. Adler, Charge disproportionation in iron(IV) oxides: Electronic properties and magnetism in $Sr_3Fe_{2-x}Ti_xO_{7-y}$ annealed at high oxygen pressures, J. Mater. Chem. **9**, 471 (1999).
[86] J. Heyd, G. E. Scuseria, and M. Ernzerhof, Hybrid functionals based on a screened Coulomb potential, J. Chem. Phys. **118**, 8207 (2003).
[87] J. Heyd, G. E. Scuseria, and M. Ernzerhof, Erratum: "Hybrid functionals based on a screened Coulomb potential" [J. Chem. Phys. **118**, 8207 (2003)]; **124**, 219906 (2006).
[88] G. Kresse and J. Furthmüller, Efficient iterative schemes for ab initio total-energy calculations using a plane-wave basis set, Phys. Rev. B **54**, 11169 (1996).